PHYSICAL REVIEW A **66**, 012501 (2002)

Photoionization of mercury: A relativistic time-dependent density-functional-theory approach

D. Toffoli,* M. Stener, and P. Decleva
Dipartimento di Scienze Chimiche, Università di Trieste, Via L. Giorgieri 1, I-34127 Trieste, Italy

(Received 22 February 2002; published 2 July 2002)

The relativistic time-dependent density functional theory (RTDDFT) has been applied to the photoionization of mercury in the energy range from the threshold up to 300 eV, thus covering almost all the photon energy range for which experimental data are available. Partial cross sections and asymmetry parameter profiles for the $6s$, $5d$, $5p$, and $4f$ subshells have been calculated and compared with earlier relativistic random-phase approximation and RTDDFT theoretical calculations and with the experimental results. A study of the spin polarization of photoelectrons from the outer subshells $6s$ and $5d$ at RTDDFT level is also presented. The use of the LB94 exchange-correlation potential together with an implementation of the RTDDFT equations in a *B*-spline basis set based on a noniterative procedure for the calculation of the induced response potential has permitted the study, at RTDDFT level, of the autoionization resonances converging to the $5d_{3/2,5/2}$ and $5p_{1/2,3/2}$ thresholds. Comparison of the RTDDFT results with the other theoretical and experimental data available confirms the effectiveness of the method in the description of correlation and relativistic effects in the photoionization of such a heavy system.

DOI: 10.1103/PhysRevA.66.012501 PACS number(s): 31.15.Ew

I. INTRODUCTION

From the experimental point of view, interest in the photoionization of atoms and molecules has grown in recent years due to the availability of tunable radiation sources. The ever increasing availability of experimental data of increased accuracy has made photoelectron spectroscopy a unique tool for the study of electron correlation and of relativistic effects in many-body systems.

In the past two decades, in the atomic field, two theoretical approaches have been extensively used for the interpretation of the experimental results. These are the random-phase approximation (RPA) [1] and the time-dependent density-functional theory (TDDFT) [2], as well as their relativistic generalizations, namely, relativistic RPA (RRPA) [3] and relativistic TDDFT (RTDDFT) [4]. These theoretical approaches, formally identical, include the spin-orbit interaction and an important class of correlation effects naturally in a relativistic framework, thus allowing the correct interpretation of, at least, the gross features of the experimental data such as partial and total cross sections, asymmetry parameters profiles, pure relativistic features such as branching ratios between fine-structure components, and spin polarization of photoelectrons.

Recently [5] we have implemented the RTDDFT equations in a finite basis set, with a noniterative algorithm for the calculation of the response induced potential. Together with the use of an exchange-correlation (XC) potential, which exhibits a correct asymptotic behavior, this algorithm has been successfully applied to the xenon atom, thus highlighting its profitable applications to heavy atom systems. Infact the finite basis set approach employed for the resolution of the RTDDFT equations should be easily extended to molecular systems allowing the evaluation of relativistic effects in molecular photoionization, a subject barely treated until now.

Before generalizing the RTDDFT formalism to the molecular case, we felt it to be important to test the algorithm on mercury, the heaviest closed-shell atom, which is the ideal system on which theoretical approaches including electronic correlation effects as well as relativistic spin-orbit effects have to be tested. The large amount of theoretical and experimental studies already existing in the literature permit a fruitful comparison with the present calculation. In the following, total, partial photoionization cross sections and asymmetry parameter profiles for the $6s$, $5d$, $5p$, and $4f$ subshells and branching ratios between fine-structure components are presented in a wide photon energy range, from threshold up to 300 eV, thus covering almost the entire photon energy range for which experimental data are available from the literature. Comparison is made with the available experimental data and with a nonrelativistic TDDFT calculation, in order to assess the relative importance of relativistic effects in such a heavy system.

In addition, at RTDDFT level, spin-polarization parameters have been calculated for the $6s$ and $5d_{3/2,5/2}$ subshells and a comparison between the RTDDFT results, those calculated at the RRPA level, and the experimental ones is presented. In the final section, a detailed analysis of the autoionization resonances converging at the $5d_{3/2,5/2}$ and $5p_{1/2,3/2}$ thresholds is presented and a comparison is made with respect to the existing theoretical calculations and experimental measurements, where available from the literature.

II. THEORETICAL METHOD

In this section we briefly outline the relativistic density functional theory (RDFT) approaches employed for the calculation of the various photoionization dynamical parameters. The two possible approaches, namely, the relativistic Kohn-Sham (RKS) approach and the RTDDFT one, are described separately, in order to point out their intrinsic differ-

---

*Author to whom correspondence should be addressed. Email address: toffoli@univ.trieste.it

ences. For further details concerning the implementation of the RTDDFT equations, interested readers are referred to Ref. [5] and references therein.

A. The relativistic Kohn-Sham approach

In the RDFT formulation [6], the description of the ground state of a closed-shell N-electron atom is obtained from the self-consistent-field (SCF) solution of the set of single-particle Dirac-Kohn-Sham equations, which take the following form:

$$h_{\mathrm{DKS}}\varphi_i=\varepsilon_i\varphi_i, \quad i=1,\ldots,N, \tag{1}$$

where

$$h_{\mathrm{DKS}}=c\alpha\cdot p+(\beta-1)c^2+V_{\mathrm{eff}}[\rho,r] \tag{2}$$

is the Hamiltonian, sum of the free particle Dirac Hamiltonian and a central potential $V_{\mathrm{eff}}[\rho,r]$, which is given by (a.u. are used throughout this paper)

$$V_{\mathrm{eff}}[\rho,r]=-\frac{Z}{r}+\int\frac{\rho(\vec{r}\,')}{|\vec{r}-\vec{r}\,'|}d\vec{r}\,'+V_{\mathrm{XC}}[\rho,r]. \tag{3}$$

The particle density $\rho(r)$ is given by

$$\rho(r)=\sum_{i=1}^{N}u_i^{+}(\vec{r})\cdot u_i(\vec{r}). \tag{4}$$

By using the standard representation for the Dirac matrices α and β, the bispinor wave functions $u_i(\vec{r})\equiv u_{n\kappa m}(\vec{r})$ are written as

$$u_{n\kappa m}(\vec{r})=\frac{1}{r}\begin{pmatrix} ig_{n\kappa}(r)\Omega_{\kappa m}(\hat{r})\\ f_{n\kappa}(r)\Omega_{-\kappa m}(\hat{r})\end{pmatrix}, \tag{5}$$

where the radial wave functions $g_{n\kappa}(r)$ and $f_{n\kappa}(r)$ are known as the *large* and *small* components. Here the angular functions are spinor spherical harmonics, given in terms of spherical harmonics $Y_{lm}(\hat{r})$ and two-component spinors χ_λ by

$$\Omega_{\kappa m}(\hat{r})=\sum_{\lambda}\langle lm-\lambda,1/2\lambda|(l1/2)jm\rangle Y_{l,m-\lambda}(\hat{r})\chi_\lambda. \tag{6}$$

In Eq. (5), n is the principal quantum number, κ and m are the angular quantum numbers: $\kappa=\mp(j+\frac{1}{2})$ for $j=l\pm\frac{1}{2}$, where j and l are the total and orbital angular momentum of the upper component. The latter also determines the parity, which is $(-I)^l$, while m is the z component of the total angular momentum.

As already stated, the relativistic KS equations (1) are solved iteratively, starting from an initial estimate of the particle density; the eigenfunctions are then updated on each loop until convergence is reached. The Hamiltonian (2) has to be fixed with a particular choice of the term V_{xc}. We have employed the LB94 as V_{xc} potential [7]: this choice was determined by the requirement of the correct asymptotic behavior (Coulomb tail $-1/r$ at large distance) in order to have bound virtual states. Once the Dirac-KS equations have been iteratively solved, the unbound photoelectron wave function must be determined as a solution of the following homogeneous equation:

$$(h_{\mathrm{DKS}}-E)\varphi=0, \tag{7}$$

where $E=c\sqrt{p^2+c^2}$, p being the photoelectron momentum, c the speed of light ($c\cong 137.035\,989\,5$ a.u.), and h_{DKS} is the SCF-Dirac-KS Hamiltonian. Finally, partial cross sections and angular asymmetry parameters for the $(n\kappa)$ subshells are computed [3]:

$$\sigma_{n\kappa}(\omega)=\frac{4\pi^2}{3c}\,\omega(|D_{j\to j-1}|^2+|D_{j\to j}|^2+|D_{j\to j+1}|^2), \tag{8}$$

$$\begin{aligned}\beta_{n\kappa}(\omega)=\Bigg[&\frac{1}{2}\,\frac{(2j-3)}{2j}|D_{j\to j-1}|^2\\ &-\frac{3}{2j}\left(\frac{2j-1}{2(2j+2)}\right)^{1/2}(D_{j\to j-1}D^{*}_{j\to j}+\text{c.c.})\\ &-\frac{(2j-1)(2j+3)}{(2j)(2j+2)}|D_{j\to j}|^2\\ &-\frac{3}{2}\left(\frac{(2j-1)(2j+3)}{2j(2j+2)}\right)^{1/2}(D_{j\to j-1}D^{*}_{j\to j+1}+\text{c.c.})\\ &+\frac{1}{2}\,\frac{(2j+5)}{(2j+2)}|D_{j\to j+1}|^2\\ &+\frac{3}{(2j+2)}\left(\frac{2j+3}{2(2j)}\right)^{1/2}(D_{j\to j}D^{*}_{j\to j+1}+\text{c.c.})\Bigg]\\ &\times(|D_{j\to j-1}|^2+|D_{j\to j}|^2+|D_{j\to j+1}|^2)^{-1},\end{aligned} \tag{9}$$

where ω is the photon energy, and $D_{j\to\bar{j}}$ are the dipole matrix elements between the initial and final states with total angular momentum of j and $\bar{j}$, respectively. The total cross section is then computed summing over initial (nk) states:

$$\sigma(\omega)=\sum_{n\kappa}\sigma_{n\kappa}(\omega). \tag{10}$$

The other photoionization dynamical parameters are associated with the spin polarization of photoelectrons. Photoelectrons are usually spin polarized due to the spin-orbit interaction in the final ionic state and in the continuum for the outgoing electron waves. According to the general treatment made by Huang [8], spin polarization of the photoelectrons is best studied in a special coordinate system, xyz, obtained after a rotation with the Euler angles $(\phi,\theta,0)$ on a fixed frame XYZ, whose Z axis is in the direction of the photon flux (see Fig. 1). The rotated coordinate system xyz is chosen such that the z axis, making an angle θ with the Z axis, is oriented along the photoelectron momentum $\vec{p}$, whereas the y axis in the direction defined by $[\vec{Z}\times\vec{z}]$. In such a reference system, for an arbitrarily polarized radiation, the three components of the spin-polarization vector of the photoelectrons, P_x, P_y,

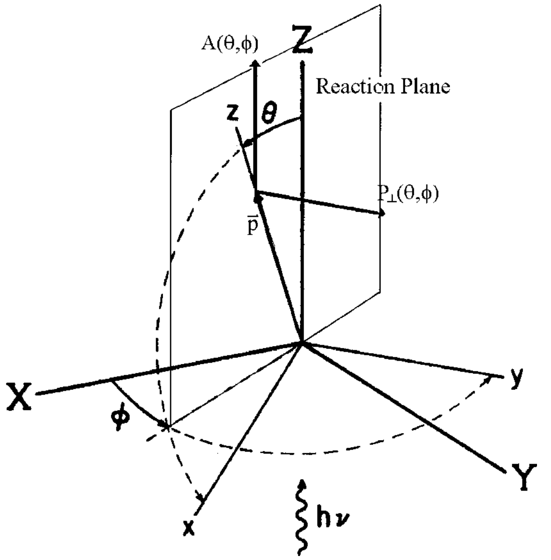

FIG. 1. Geometrical relationships used in spin-polarization formulas. The photon is incident along the Z axis and the photoelectron is ejected along the z axis.

and P_z are given in terms of three dynamical parameters $\overline{\xi}$,[1] (see footnote 1) η, and ζ according to [8]

$$P_x(\theta,\phi)=\lfloor \eta[-S_1\sin(2\phi)+S_2\cos(2\phi)] + \overline{\xi}S_3\rfloor\sin(\theta)/F(\theta,\phi),$$

$$P_y(\theta,\phi)=\eta[1-S_1\cos(2\phi) - S_2\sin(2\phi)]\sin(\theta)\cos(\theta)/F(\theta,\phi), \quad (11)$$

$$P_z(\theta,\phi)=\zeta S_3\cos(\theta)/F(\theta,\phi),$$

where

$$F(\theta,\phi)=1-\tfrac{1}{2}\beta\lfloor P_2(\cos[\theta])+\tfrac{3}{2}[S_1\cos(2\phi) + S_2\sin(2\phi)]\sin^2(\theta)\rfloor.$$

$\overline{\xi}$, η, and ζ are energy-dependent parameters and S_i , $i=1$, 3, are the Stokes parameters which specify the polarization of the given photon beam. Specializing to pure circularly polarized photons or to linear polarization they assume the following values [8]: (1) $S_1=S_2=0$, $S_3=\pm1$ ($+1$ for right circular polarization, -1 for left circular polarization); (2) $S_1=\pm1$, $S_2=S_3=0$ ($+1$ and -1 for linear polarization along the Y and X axes, respectively). Like partial cross sections and asymmetry parameters, $\overline{\xi}$, η, and ζ are given in term of the dipole amplitudes $D_{j\to\overline{j}}$ [8],

$$\begin{aligned}\overline{\xi}_{n\kappa}(\omega)=(-)^{l+j+1/2}\Bigg[&-\frac{3(2j-1)}{4(2j)}|D_{j\to j-1}|^2\\ &-\frac{3(2j+1)}{2(2j)(2j+2)}|D_{j\to j}|^2+\frac{3(2j+3)}{4(2j+2)}|D_{j\to j+1}|^2\\ &+\frac{3}{4(2j)}\left(\frac{(2j-1)(2j+2)}{2}\right)^{1/2}\\ &\times(D_{j\to j-1}D^*_{j\to j}+\text{c.c.})-\frac{3}{4(2j+2)}\\ &\times\left(\frac{(2j)(2j+3)}{2}\right)^{1/2}(D_{j\to j}D^*_{j\to j+1}+\text{c.c.})\Bigg]\\ &\times(|D_{j\to j-1}|^2+|D_{j\to j}|^2+|D_{j\to j+1}|^2)^{-1}, \quad (12)\end{aligned}$$

$$\begin{aligned}\eta_{n\kappa}(\omega)=i(-)^{l+j+1/2}\Bigg[&-\frac{3}{4}\left(\frac{(2j-1)}{2(2j+2)}\right)^{1/2}(D_{j\to j-1}D^*_{j\to j}\\ &-\text{c.c.})+\frac{3}{4}\left(\frac{(2j-1)(2j+3)}{2j(2j+2)}\right)^{1/2}(D_{j\to j-1}D^*_{j\to j+1}\\ &-\text{c.c.})-\frac{3}{4}\left(\frac{(2j+3)}{2(2j)}\right)^{1/2}(D_{j\to j}D^*_{j\to j+1}-\text{c.c.})\Bigg]\\ &\times(|D_{j\to j-1}|^2+|D_{j\to j}|^2+|D_{j\to j+1}|^2)^{-1}, \quad (13)\end{aligned}$$

$$\begin{aligned}\zeta_{n\kappa}(\omega)=\Bigg[&-\frac{3}{2(2j)}|D_{j\to j-1}|^2+\frac{3}{(2j)(2j+2)}|D_{j\to j}|^2\\ &+\frac{3}{2(2j+2)}|D_{j\to j+1}|^2\\ &-\frac{3}{2(2j)}\left(\frac{(2j-1)(2j+2)}{2}\right)^{1/2}(D_{j\to j-1}D^*_{j\to j}\\ &+\text{c.c.})-\frac{3}{2(2j+2)}\left(\frac{2j(2j+3)}{2}\right)^{1/2}(D_{j\to j}D^*_{j\to j+1}\\ &+\text{c.c.})\Bigg](|D_{j\to j-1}|^2+|D_{j\to j}|^2+|D_{j\to j+1}|^2)^{-1}.\end{aligned} \quad (14)$$

From Eq. (11) it is worth noting that for linear polarized (or unpolarized) light only the η parameter can be measured, whereas when circularly polarized photons are used, every component of the spin-polarization vector corresponds to a dynamical parameter. In order to make contact with the experimental measured quantities it is useful to define an equivalent set of spin-polarization parameters A, α, and ξ in terms of those defined in Eqs. (12)–(14):

$$\xi=\eta/2,$$

$$A=-\tfrac{1}{3}(2\overline{\xi}-\zeta), \quad (15)$$

$$\alpha=-\tfrac{2}{3}(\overline{\xi}+\zeta).$$

---

[1] In Ref. [8] the parameter $\overline{\xi}$ is denoted by ξ.

When pure circularly polarized photons are used, the spin-polarization parameters A and α specify completely the component of the spin-polarization vector along the photon momentum [$A(\theta,\phi)$ in Fig. 1], which is given by

$$A(\theta,\phi)=\pm\frac{A-\alpha P_2(\cos\theta)}{1-1/2\beta P_2(\cos\theta)}=A(\theta), \tag{16}$$

where the + and − signs apply to right and left circular polarization, respectively.

In Eq. (16) the A parameter represent the total spin polarization, directed along the photon momentum, whereas α is related to the angular dependence of $A(\theta)$. As usual, $P_2(\cos\theta)$ is the Legendre polynomial of second degree. The ξ parameter is instead related to the component of the spin-polarization vector along the y axis, denoted as $P_\perp(\theta,\phi)$ in Fig. 1 because it is perpendicular to the (z,Z) plane (reaction plane). For circularly polarized or unpolarized light $P_\perp(\theta,\phi)$ is given by

$$P_\perp(\theta,\phi)=\frac{2\xi\sin(\theta)\cos(\theta)}{1-\frac{1}{2}\beta P_2(\cos\theta)}=P_\perp(\theta). \tag{17}$$

B. The relativistic time-dependent density-functional theory

The present RTDDFT procedure starts with the calculation of the first-order perturbations on the Dirac-Kohn-Sham eigenfunctions $\varphi_i^{(1,\pm)}$, which according to the modified Sternheimer approach [9] are solutions of the following inhomogeneous equations:

$$[h_{\mathrm{DKS}}-\varepsilon_i\pm\omega]\varphi_i^{(1,\pm)}=\sum_m (1-n_m)\varphi_m\langle m|\Phi^{\mathrm{SCF}}|i\rangle. \tag{18}$$

Here Φ^{SCF} is the SCF potential which is given by

$$\Phi^{\mathrm{SCF}}(\vec{r},\omega)=\Phi^{\mathrm{EXT}}(\vec{r},\omega)+\int\frac{\delta\rho(\vec{r}\,',\omega)}{|\vec{r}-\vec{r}\,'|}d\vec{r}\,' +\left.\frac{\partial V_{\mathrm{XC}}}{\partial\rho}\right|_{\rho(r)}\delta\rho(\vec{r},\omega). \tag{19}$$

In Eq. (19), Φ^{EXT} is the unperturbed external dipole potential while the second and third right-hand terms represent, respectively, the Coulomb and exchange-correlation potentials induced by electron redistribution. $\delta\rho$ represents the first-order perturbation of the density, which is computed from the first-order perturbed wave functions:

$$\delta\rho(\vec{r},\pm\omega)=\sum_i n_i(\varphi_i^*\varphi_i^{(1,\pm)}+\varphi_i\varphi_i^{(1,\mp)*}). \tag{20}$$

In this work we have approximated the XC response with that relative to the Vosko-Wilk-Nusair (VWN) [10] exchange-correlation potential. As stated before, the Φ^{SCF} potential is not evaluated with the usual iterative procedure but directly. The general lines of this procedure are fully explained in Ref. [5] and are not reported here. Once the SCF potential had been obtained, the RTDDFT partial cross sections, angular asymmetry parameters, and spin-polarization parameters for each subshell $(n\kappa)$ are computed with the aid of Eq. (8), (9), and (12)–(15), using Φ^{SCF} in place of the dipole operator.

III. COMPUTATIONAL DETAILS

Both homogeneous Eqs. (1), (7), and inhomogeneous Eq. (18) differential equations are recast into algebraic eigenvalue equations or linear systems by employing a finite basis set of radial B-spline functions [11,12]. The B-spline basis set is unambiguously determined by its order and the grid of knots. In this work we have employed splines of order eight and the radial grid of Ref. [13] slightly modified in the following way: the original grid is kept until the step between two adjacent knots is greater than a step which is half of the minimum wavelength of the photoelectron and afterwards it is linear with this step to a large cutoff radius. In the present work we have employed different grid parameters, according to the energy region investigated. In the near threshold region (up to 210 eV) a linear grid step of 0.125 a.u. and a cutoff radius of 30.0 a.u. proved a good choice while in the high-energy region (up to 300 eV) the former parameter was set to 0.10 a.u. The profiles have been joined at a photon energy of 210 eV. In studying the autoionization resonances converging to the $5d_{3/2,5/2}$ and $5p_{1/2,3/2}$ thresholds the linear grid step parameters were set to 0.24 and 0.16 a.u. respectively, whereas the cutoff radius was set to 25.0 a.u. in the latter case for computational economy. The nonrelativistic TDDFT results have been obtained using B splines of order eight and a grid of knots as suggested by Froese Fischer, Guo, and Shen [14] slightly modified as described in [15]. The linear grid step was set to 0.100 a.u. whereas the large cutoff radius was set to 30 a.u. In Eq. (18), h_{DKS}, ε_i, and φ_i are obtained from a Dirac-KS calculation for the ground state in the B-spline basis set, employing the LB 94 [7] exchange-correlation potential. In Eq. (18) we employed the experimental ionization potentials instead of ε_i, in order to have better agreement with the experiment. In the nonrelativistic TDDFT calculation the ionization potentials have been averaged according to the relative population of the spin-orbit fine-structure components.

IV. RESULTS AND DISCUSSION

A. Total and partial cross sections

The total RTDDFT photoionization cross section of Hg versus the incident photon energy is reported in Fig. 2 up to 300 eV together with a nonrelativistic TDDFT calculation. The opening of the various photoionization channels is preceded, in the theoretical profiles, by a very rich series of autoionization resonances. The energy intervals from the threshold (at 10.438 eV) to the $^2D_{5/2}$ one (at 14.841 eV) and between the two $^2D_{3/2,5/2}$ spin-orbit split thresholds ($^2D_{3/2}$ threshold at 16.705 eV) are characterized by features associated with discrete excitations of a bound $5d$ electron. The opening of the $5p_{1/2,3/2}$ photoionization channels ($^2P_{3/2,1/2}$ thresholds at 71.7 and 90.3 eV, respectively) are preceded by

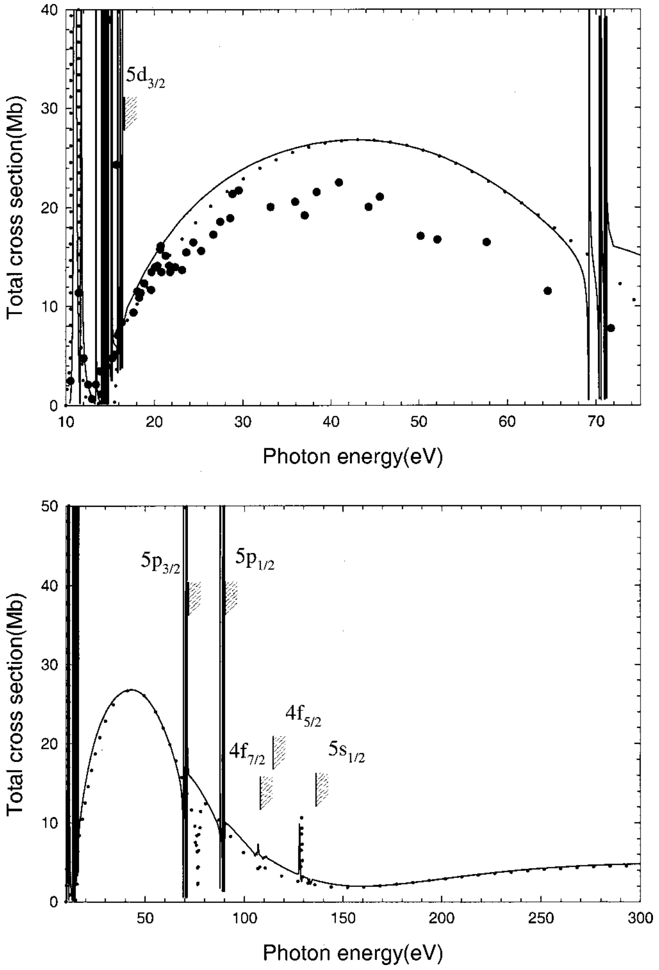

FIG. 2. Hg total photoionization cross-section profile: full curve, RTDDFT; dotted curve, TDDFT result; closed circles, experimental data from Ref. [16].

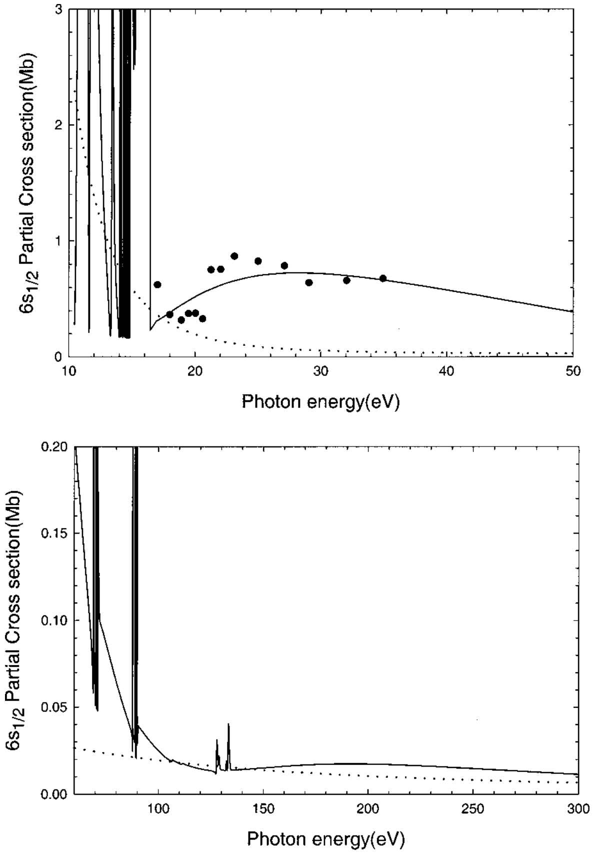

FIG. 3. Hg $6s$ partial photoionization cross-section profiles. Theory: solid lines, RTDDFT; dotted lines, RKS. Experimental data: solid circles from Ref. [20].

autoionization resonances due to excitations of a $5p$ electron to $ns_{1/2}$ and $n'd_{3/2,5/2}$ Rydberg states. Autoionization resonances converging to the $4f_{7/2,5/2}$ and $5s_{1/2}$ thresholds at 107.1, 111.1, and 134.0 eV, respectively, are visible in the theoretical RTDDFT profile but have not been investigated in detail, since no experimental data are available. In the upper panel of Fig. 2 the theoretical results are compared with the available experimental data of Cairns, Harrison, and Schoen [16]. According to Dehmer and Berkowitz [17] the experimental data of Cairns, Harrison, and Schoen were scaled by a factor of 0.5 thus providing ±30% accuracy. As can be seen from Fig. 2, the theoretical cross sections rise steadily from the $5d$ thresholds (due to centrifugal barrier effects on the dominant $5d \rightarrow f$ orbital wave functions) and after reaching a maximum near 40 eV of photon energy, gradually decrease, a behavior displayed also by the other elements of the IIB group [18]. As can be seen from the upper panel of Fig. 2, the agreement between theoretical RTDDFT and experimental results is quite good only for a few eV's above the $^2D_{3/2}$ ionization threshold. Infact, from about 22 eV to the entire energy range experimentally explored, the experimental points lies systematically below the theoretical profile. These RTDDFT results are in good agreement with previous RRPA calculations [18,19], whereas a slightly better agreement with the experiment is obtained with a RRPA calculation which includes the relaxation effects (RRPAR) [19]. These findings confirm that the discrepancies observed between our RTDDFT calculation and the experiment cannot be ascribed entirely to difficulties associated with absolute cross-section measurements but they are also due, to some extent, to the importance of relaxation and multielectron effects neglected at the RRPA or RTDDFT level. The comparison between the RTDDFT results and the analog nonrelativistic TDDFT results suggests that relativistic effects does not alter dramatically the behavior of the total cross section, at least in nonresonant regions.

The RTDDFT partial cross-section profile for the $6s_{1/2}$ subshell is reported in Fig. 3 along with the available experimental results [20] and with a RKS calculation which neglects interchannel coupling. As stated above, the opening of the $5d_{3/2}$ photoionization channels is preceded by a very rich autoionization series converging to the $^2D_{3/2}$ threshold. After that, the partial cross section rises steadily reaching a maximum at about 28 eV in fair accord with the experiment. The present RTDDFT results agree with earlier RRPA [18] and RTDDFT [21] calculations. It has to be noted that in the energy region between the $^2D_{3/2}$ threshold and about 24 eV, the experimental data are affected by a severe scattering suggesting a minimum at about 20 eV ascribed to a Cooper minimum [17,20]. Actually, neither with the RRPA [18] nor

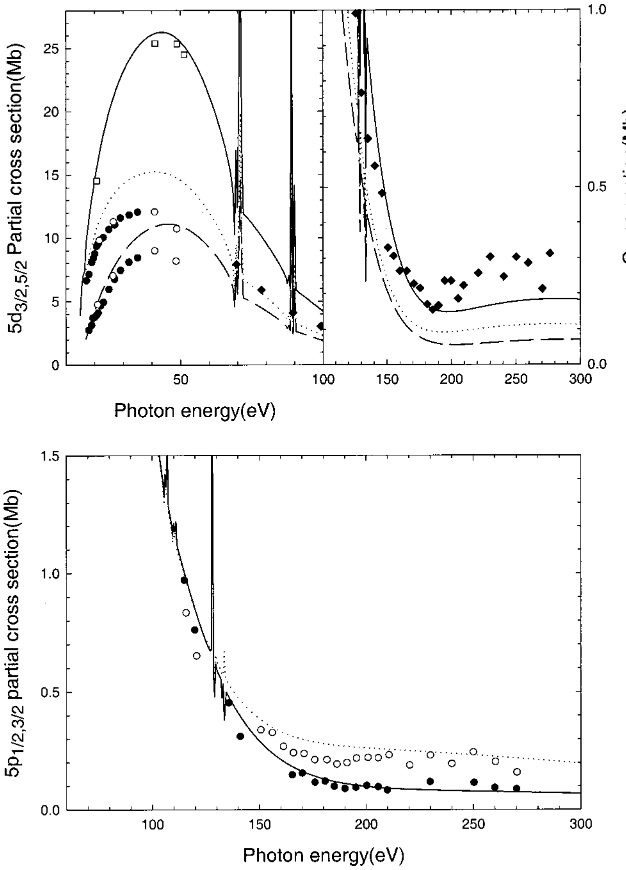

FIG. 4. *Upper panel*. Theory: $5d$ total cross section (solid line), $5d_{5/2}$ partial cross section (dotted line), $5d_{3/2}$ partial cross section (dashed line) in the RTDDFT. Experiment: open squares and closed diamonds represent $5d$ total cross section of Refs. [26] and [27], respectively. Closed circles and open circles represent partial cross-section measurements of Refs. [20] and [17], respectively. *Lower panel*. Hg $5p_{1/2,3/2}$ partial cross-section profiles. Theory: solid line, RTDDFT $5p_{1/2}$ partial cross section; dotted line, RTDDFT $5p_{3/2}$ partial cross section. Experiment: closed and open circles are the $5p_{1/2,3/2}$ partial cross sections from Ref. [27].

the RTDDFT [21] approaches has a Cooper minimum been detected above the $^2D_{3/2}$ threshold. In this context it might be of interest to note that in the energy region from the $^2D_{3/2}$ threshold to ≈24 eV a great number of resonances attributed to two-electron excitations had been observed in absorption measurements [22] together with the appearance of satellites in the photoelectron spectra [23,24], which are believed to reflect $6p^2$ admixtures in the $6s^2$ ground state, with $^2P_{1/2}$ and $^2P_{3/2}$ final ionic states. It was observed [25] that both the $6p$ ($^2P_{3/2}$ final ionic state) and $6s$ cross sections are considerably modulated at wavelengths where two-electron resonances appear. Two-electron excitations are not accounted for by RRPA or RTDDFT approaches and these modulation effects might be responsible for a theoretically unexpected minimum in the cross section and, in general, for the scattering in the $6s$ partial cross-section data reported in [20]. Further experimental investigations in this energy range are needed in order to establish the effects into the main-line photoionization channels, of multielectronic processes neglected at RTDDFT or RRPA level. The comparison between the RTDDFT and RKS calculations reveals that inclusion of interchannel coupling with the strongest $5d$ photoionization channels is needed in order to achieve good accord with the experimental data above the $5d$ thresholds. Infact the RTDDFT $6s$ partial cross section reaches a maximum of about 0.7 Mb at ≈28 eV of photon energy followed by a minimum at about 130 eV, in complete disagreement with the single-channel RKS calculation. However, the position of the minimum is difficult to determine with accuracy because it is very close to the $5s$ threshold.

The $5d_{3/2,5/2}$ RTDDFT partial cross sections are reported in the upper panel of Fig. 4 along with the experimental data available [17,20,26,27]. The RTDDFT total $5d$ photoionization cross section is in good agreement with the experimental measurements of Süzer *et al.* [26] and with RRPA calculations [18,19] but in disagreement with a RRPAR calculation of Kutzner *et al.* [19]. Relaxation effects are more apparent in the partial cross sections, where, despite the good accord with the experimental results of Shannon and Codling [20] until few eV's above the $5d$ thresholds, both RTDDFT and RRPA [18,19] profiles are significantly larger than the experimental values at higher energies whereas a RRPAR [19] calculation shows a better, although not completely satisfactory, accord with the experiments. These findings highlight both the role of relaxation and multielectronic effects in the near threshold energy range and the necessity of experimental data of improved accuracy which may allow a clearer evaluation of the former. It is interesting also to note that the RTDDFT profiles display a clear Cooper minimum around 190 eV, in good agreement with the experimental data of Lindle *et al.* [27], whereas it is not so apparent in RRPA [28] and in Dirac-Slater [29] calculations.

The RTDDFT partial $5p_{3/2,1/2}$ photoionization cross sections are reported in the lower panel of Fig. 4 along with the experimental data of Lindle *et al.* [27], which include the important corrections on previous measurements of Kobrin *et al.* [29] for the increased quantum yield of the sodium salicylate detector at higher energies. Both the theoretical partial cross sections are in good agreement with the experiment and with previous RRPA calculations [28].

Finally, the RTDDFT $4f$ total photoionization cross section and partial $4f_{7/2,5/2}$ photoionization cross sections are reported in Fig. 5 along with the total $4f$ experimental cross section of Lindle *et al.* [27]. Both experimentally and theoretically, the delayed onset of the $4f$ cross section is apparent due to a large centrifugal barrier acting on the εg continua. The RTDDFT results resemble closely the RRPA [19,28] ones and appear substantially overestimated with respect to the experimental data above the cross-section minimum at about 140 eV although its position and the general shape of the experimental profile are rather well accounted for. The reasons of this discrepancy are essentially twofold. First, the absolute scale of the cross-section measurements could be off by as much as 30% [17], possibly explaining much of the discrepancy with both RTDDFT and RRPA. Second, the inclusion of relaxation effects at the RRPAR level [19] improves the agreement with the experimental data partly due to the inclusion of overlap integrals, which account, in an

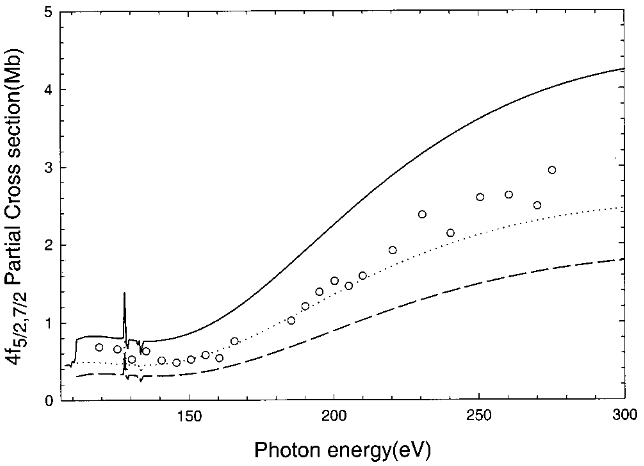

FIG. 5. Theory: $4f$ total cross section (solid line), $4f_{7/2}$ partial cross section (dotted line), $4f_{5/2}$ partial cross section (dashed line) in the RTDDFT. Experiment: open circles represent $4f$ partial cross section of Ref. [27].

energy-independent manner, for the transfer of oscillator strength from the main-line channels to doubly excited channels. However, due to uncertainties in the absolute scale of the experimental data and the lack of experimental measurements for Hg double excitations or ionization in this energy range, a reasonable estimation of the multielectronic processes neglected at RRPA and RTDDFT levels is hindered and, therefore, further measurements should be encouraged for a correct evaluation of the performance of the RTDDFT and RRPA methods in this energy range.

B. Branching ratios between fine-structure components

The $5d_{5/2,3/2}$ branching ratio (BR) γ_{5d} is reported in the upper panel of Fig. 6, up to 300 eV along with the experimental data available from the literature [17,20,23,26,29,30]. At variance with the $5d$ partial cross sections, the accord with the experimental data is excellent in the entire energy range covered by the latter. In particular, in the near threshold region, the present RTDDFT results closely resemble the RRPA [18], RRPAR [19], and earlier RTDDFT [21] results. The behavior of the branching ratio is easily explained according to the arguments of Walker and Waber [31], from which the BR should be higher than its statistical value when partial cross sections are rising and below it when they are falling. In the high-energy region, the RTDDFT results have to be compared with an earlier RRPA calculation [28], where all the 17 relativistic channels allowed by dipole excitation from the $5d$, $5p$, and $4f$ subshells were taken into account. Both calculations predict an increase of the BR after the Cooper minimum in the partial cross section, at values higher than the statistical ratio. Then, after a maximum value of 1.7 at about 220 eV (the maximum value predicted at the RRPA level [28] is less than 1.6 at about 240 eV) the BR is seen to reach asymptotically the statistical value. Unfortunately, no experimental measurements are available in these energy regions for a fruitful comparison with the theoretical findings.

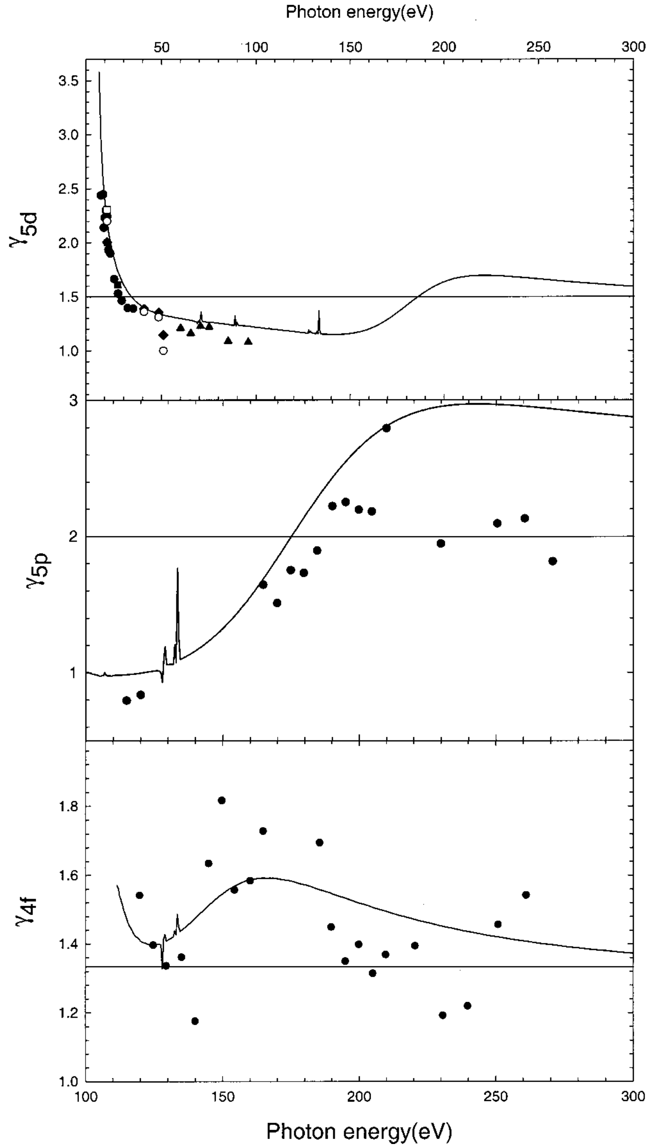

FIG. 6. *Upper panel*. Branching ratio γ for the $5d$ subshells of mercury. Theory: solid line, RTDDFT result. Experimental data: solid circles from Ref. [20], open circles from Ref. [23], closed squares from Ref. [17], open squares from Ref. [30], closed diamonds from Ref. [26], closed triangles from Ref. [29]. *Central panel*. Branching ratio for the $5p$ subshells. Theory: solid line, RTDDFT; closed circles, experimental data from Ref. [29]. *Lower panel*. Branching ratio for the $4f$ subshells. Theory: solid line RTDDFT; closed circles, experimental data from Ref. [29].

The RTDDFT BR profiles for the $5p$ and $4f$ subshells, γ_{5p} and γ_{4f}, are reported in the central and lower panel of Fig. 6, respectively, along with the experimental data of Ref. [29]. The large spin-orbit splitting of the $5p$ subshells (18.6 eV) leads to large deviations of the BR from its statistical value of 2.0 and indeed the experimental points show an increase from about 0.8 at 115 eV to 2.8 at about 210 eV. In this energy range there is a good agreement between experiment and the RTDDFT results. Infact, the RTDDFT calculation gives a branching ratio of 0.986 at 115 eV and 2.811 at 210 eV, in good accord with the experimental findings, and it is seen to be closer to the experimental data than the RRPA calculation of Johnson and Radojevíc [28] especially in the near threshold region. However both the RRPA [28] and RTDDFT calculations fail to predict the sudden drop of the BR to the statistical value of 2 experimentally seen at about 220 eV, where however the experimental data are affected by large experimental errors [29]. A further accurate experimental measurement of the $5p$ BR in this energy range will help in a fruitful comparison with the theoretical results. Finally, comparison between theoretical RTDDFT and experimental results for the $4f$ BR reveals a fairly good agreement between theory and experiment only in the near threshold region where, in accord with the experiment and with a RRPAR calculation [19], the BR is predicted higher than the statistical ratio, in disagreement with previous RRPA results [19,28]. At higher energies, the experimental data [29] are affected by a severe scattering which limit the comparison with RRPA [19,28], RRPAR [19], and RTDDFT calculations, which display the same general behavior. Again, an accurate experimental redetermination of the $4f$ BR at energies well above the thresholds should help in a critical evaluation of the theoretical results elucidating if the discrepancies observed are due to experimental accuracy or correlation effects not accounted for by the RTDDFT or RRPA approaches.

C. Asymmetry parameter profiles for 6*s*, 5*d*, 5*p*, and 4*f* subshells

The asymmetry parameter profiles for the $6s_{1/2}$ subshell and for the $5d$ spin-orbit fine-structure components are reported in the upper and lower panels of Fig. 7 respectively, along with the available experimental data from various sources [25,29,32–35]. The behavior of the asymmetry parameter for the $6s_{1/2}$ subshell as a function of photon energy has been the subject of various theoretical [18,21] and experimental studies [25,32,33,35] because of its pronounced departure from the nonrelativistic value of 2. As can be seen from the upper panel of Fig. 7, in the energy region where two electron excitations are seen to modulate the partial cross section, the experimental data show a considerable scatter around the RTDDFT results, which are similar to those of Parpia and Johnson [21] and to earlier RRPA results [18], and appear to interpolate well the experimental values. The evidence does not appear to support the presence of a minimum related to a Cooper minimum in the cross section [32]. However, as suggested in [25] features that so drastically alter the $6s$ partial cross section should also influence the other photoionization parameters such as the asymmetry parameter thus possibly explaining the scattering of the experimental data from various sources. Both RRPA [18] and RTDDFT approaches predict a minimum in the asymmetry parameter profile at about 130 eV, close to the $5s$ threshold, in correspondence with a minimum in the partial cross section. This is clearly due to interchannel couplings because it is not seen at the RKS level, which exhibit a monotonic growth up to the nonrelativistic value of 2.

In the lower panel of Fig. 7, the RTDDFT asymmetry parameter profile for the $5d_{3/2,5/2}$ fine-structure components

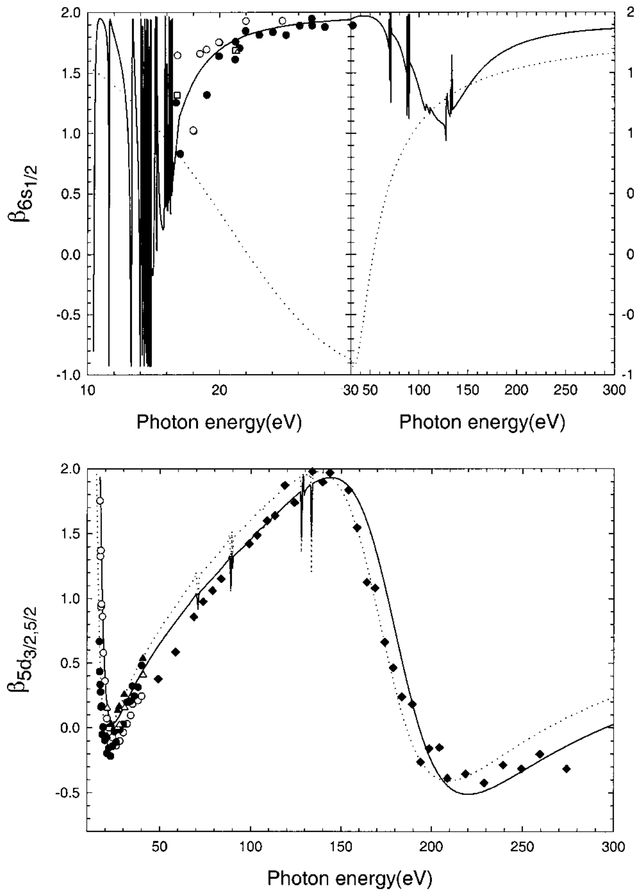

FIG. 7. *Upper panel*. Asymmetry parameter profiles for the $6s$ subshell of mercury. Theory: solid line and dotted line are the RTDDFT and RKS results, respectively. Experiment: closed circles from Ref. [32], open circles from Ref. [25], open squares from Ref. [35], open triangle from Ref. [33]. *Lower panel*. Asymmetry parameter profiles for the $5d_{3/2,5/2}$ subshells of mercury. Theory: solid line and dotted line are the RTDDFT results for the $5d_{3/2}$ and $5d_{5/2}$ subshells, respectively. Experiment: open and closed circles are the asymmetry parameter profiles of $5d_{3/2}$ and $5d_{5/2}$ subshells from Ref. [32]; open and closed triangles are the asymmetry parameter profiles of $5d_{3/2}$ and $5d_{5/2}$ subshells from Ref. [34]; closed diamonds are the $5d$ asymmetry parameter profile taken from Ref. [29].

is shown, along with the experimental data available from the literature [29,32,34]. The $5d_{3/2,5/2}$ asymmetry parameter profiles are characterized by strong oscillations within the allowed range of -1 and $+2$, due to the shape resonances and the subsequent Cooper minima in the partial cross sections. The present RTDDFT results are in rather good agreement with earlier RTDDFT [21]and RRPA [19,28] calculations and with the experimental data. At higher energies our RTDDFT results are compared with the experimental data of Kobrin *et al.* [29] and a good agreement is obtained.

We present the RTDDFT $5p_{1/2,3/2}$ asymmetry parameter profiles in the upper panel of Fig. 8, along with the experimental data of Kobrin *et al.* [29]. Both theoretically and experimentally, the asymmetry parameter profile for the two final ionic states shows substantial differences beyond that due to the kinetic-energy effect. Infact the RTDDFT $5p_{1/2}$

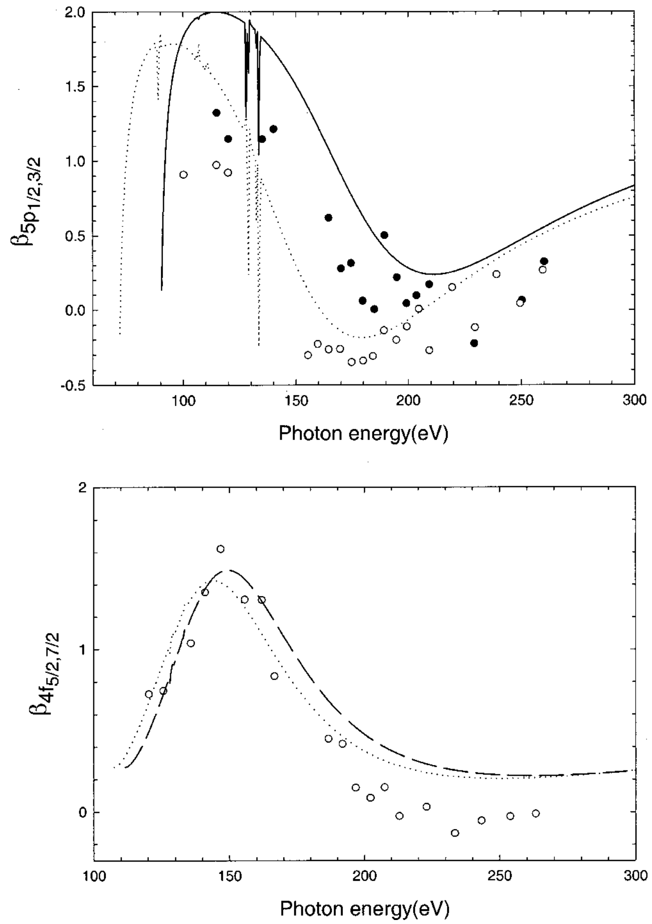

FIG. 8. *Upper panel*. Asymmetry parameter profiles for the $5p_{1/2,3/2}$ subshells of Hg. Theory: solid line and dotted line are the RTDDFT results for the $5p_{1/2}$ and $5p_{3/2}$ subshells, respectively. Experimental data: open and closed circles are the asymmetry parameter profiles of $5p_{3/2}$ and $5p_{1/2}$ subshells from Ref. [29]. *Lower panel*. Asymmetry parameter profiles for the $4f_{5/2,7/2}$ subshells of Hg. Theory: dashed line and dotted line are the RTDDFT results for the $4f_{5/2}$ and $4f_{7/2}$ subshells, respectively. Experiment: open circles are the $4f$ asymmetry parameter from Ref. [29].

asymmetry parameter drop to 0.25 at about 210 eV, while the $5p_{3/2}$ one reaches its minimum value of -0.2 at about 180 eV. Experimentally, the minimum values are close to 0 and -0.3 for the $5p_{1/2}$ and $5p_{3/2}$ subshells, respectively. The present RTDDFT results are in good agreement with an earlier RRPA calculation [28] and in fairly good accord with the experimental data especially at photon energies well after the thresholds, though the latter are rather scattered. The RTDDFT $4f_{5/2,7/2}$ asymmetry parameter profiles are reported in the lower panel of Fig. 8 with the available experimental data taken from Ref. [29]. Good accord with the experimental data is obtained up to 190 eV whereas at higher energies our results lie consistently above the former. An analogous discrepancy had been observed also in earlier RRPA [28] and RRPAR [19] calculations. A comparison with these theoretical results suggest that both RRPA [19,28] and RTDDFT predict correctly the energy position of the maximum in the asymmetry parameter profile and are in reasonable agreement with the RRPAR results [19].

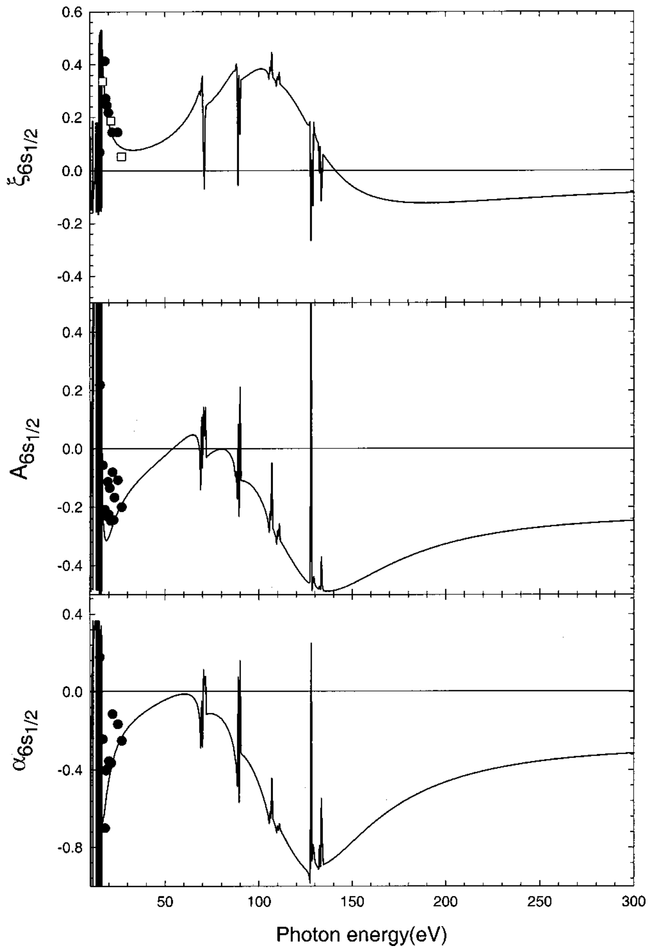

FIG. 9. Spin-polarization parameters for the $6s$ subshell of mercury. Theory: solid lines, RTDDFT results. Experimental data: closed circles from Ref. [25], open squares from Ref. [35].

D. Spin-polarization parameters profiles for 6*s* and 5*d* subshells

We have reported the RTDDFT profiles of the spin-polarization parameters ξ, A, and α for the $6s_{1/2}$ and $5d_{3/2,5/2}$ subshells in Figs. 9 and 10, respectively, along with the experimental results [25,35–37].

The RTDDFT results for the $6s$ subshell (Fig. 9) are in good agreement with the corresponding RRPA results of Ref. [18] and display for all the parameters a strong deviation from the nonrelativistic value of zero in the entire energy range experimentally explored. This behavior was, however, anticipated from the analysis of the energy dependence of the asymmetry parameter profile, which highlights the importance of the relativistic spin-orbit effects. The general energy dependence of all photoionization parameters is rather well accounted for by the present RTDDFT calculation, though the experimental data [25,35] show some scattering which might be caused by the presence of resonances attributed to two-electron excitations [25] and which are not accounted for by the present RTDDFT approach. A strong energy dependence is predicted for all the spin-polarization parameters in the energy region of the minimum in the $6s$ partial cross section at about 130 eV. Also strong autoionization features,

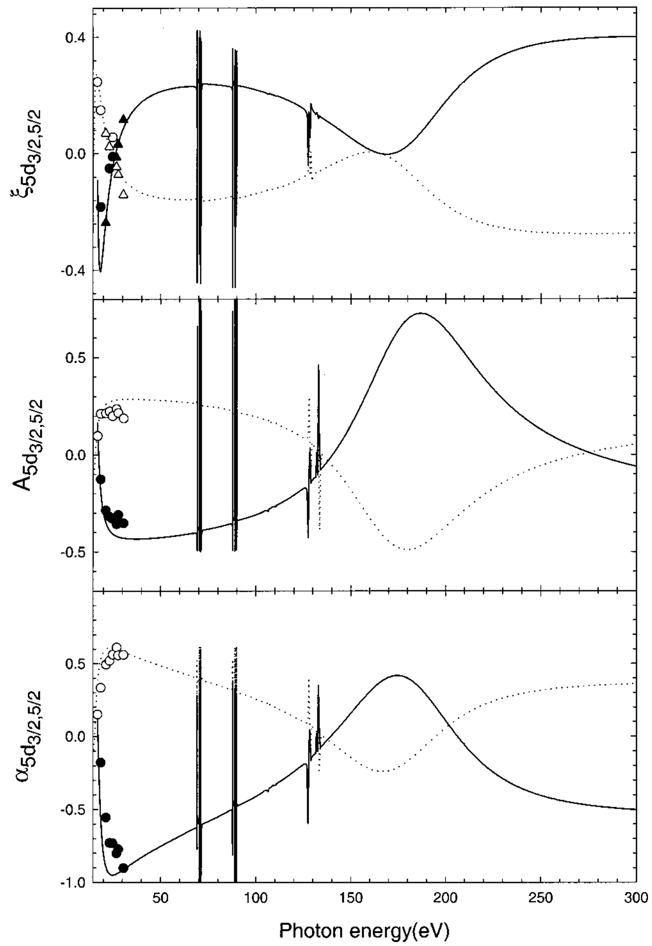

FIG. 10. Spin polarization parameters for the $5d_{3/2,5/2}$ subshells of mercury. Theory: solid lines and dotted lines are the RTDDFT results for the $5d_{3/2}$ and $5d_{5/2}$ subshells, respectively. Experimental data: closed and open circles represent the $5d_{3/2}$ and $5d_{5/2}$ spin-polarization parameters taken from Ref. [37]; closed and open triangles represent the $\xi\ 5d_{3/2}$ and $\xi\ 5d_{5/2}$ spin-polarization parameter taken from Ref. [36].

predicted by the present approach, are superimposed on the nonresonant profile. Unfortunately, to our knowledge, no experimental data exist in this energy region.

The accord between experimental data [36,37] and RTDDFT results is rather good for the spin-polarization parameters associated with photoionization from the $5d$ subshells (see Fig. 10). Near the thresholds there is a strong energy dependence of all the spin-polarization parameters due to the shape resonance in the $5d\rightarrow\varepsilon f$ photoionization channels, and another one is clearly associated with the occurrence of a Cooper minimum at about 190 eV. Unfortunately, no experimental data are, to our knowledge, available for a comparison with the RTDDFT results in the high-energy region, far from the $5d$ thresholds.

E. Autoionization resonances converging to the $^2D_{3/2,5/2}$ thresholds

Starting from the first ionization threshold ($^2S_{1/2}$), at 10.438 eV of photon energy, the photoionization cross section of mercury is dominated by pronounced autoionization resonances due to excitation of d electrons into discrete states beyond the photoionization threshold, which are energetically degenerate with continuum states. There are six Rydberg series of autoionizing states converging to the $^2D_{3/2}$ and $^2D_{5/2}$ thresholds of Hg$^+$:

$$\mathrm{Hg}\quad 5d^96s^2(^2D_{5/2})np_{3/2},nf_{5/2},nf_{7/2},$$

$$\mathrm{Hg}\quad 5d^96s^2(^2D_{3/2})np_{1/2},np_{3/2},nf_{5/2}.$$

These intermediate states decay into either the $6s\varepsilon p_{1/2}$ or $6s\varepsilon p_{3/2}$ continua for photon energies below the $^2D_{5/2}$ threshold, whereas the region between the $^2D_{3/2,5/2}$ thresholds is characterized by autoionizing levels which interact with the partial continua of two final ionic states Hg$^+$ $^2S_{1/2}$ and Hg$^+$ $^2D_{5/2}$, giving rise to photoelectrons of different kinetic energy. The total RTDDFT photoionization cross section in this energy region is reported in the upper panel of Fig. 11 together with the experimental data of Brehm [38]. Above the

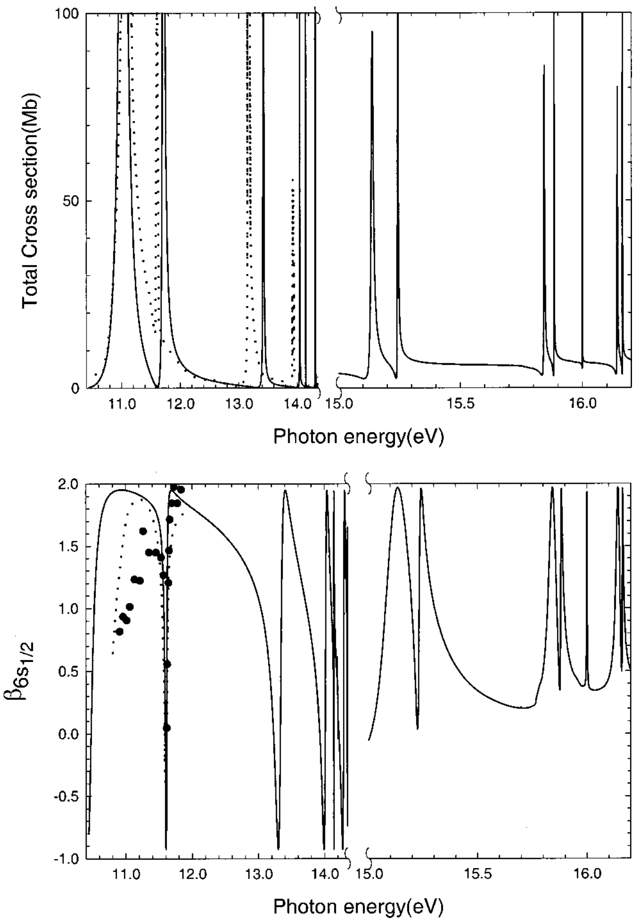

FIG. 11. *Upper panel*. Total photoionization cross-section profile in the autoionization region of $5d^9(^2D_{3/2})np_{1/2,3/2}n'f_{5/2}$ ($n=6-9,n'=5$) and $5d^9(^2D_{5/2})n''p_{3/2}$ ($n''=7,8$) configurations. Solid line, RTDDFT result; dotted line, experimental data from Ref. [38]. *Lower panel*. Angular distribution asymmetry parameter profile for the $^2S_{1/2}$ state of Hg$^+$ in the same spectral region. Solid line, RTDDFT result; dotted line, experimental data from Ref. [43]; closed circles, experimental data from Ref. [42].

$^2S_{1/2}$ threshold, the first two strong resonances are associated with the discrete excitations Hg $5d^96s^2(^2D_{3/2})6p_{1/2},p_{3/2}$, while at photon energies between 13 and 14 eV s two resonances of the same Rydberg series Hg $5d^96s^2(^2D_{5/2})np_{3/2}$ for $n=7$, 8 appear. We also observe two further resonances at 14.143 35 and 14.1437 eV associated with the closed channels $5d^96s^2(^2D_{5/2})$ $5f_{5/2}$, $5f_{7/2}$, in fair accord with the absorption measurements of Mansfield [22], who located these features at 13.973 and 13.976 eV, respectively, with a splitting of about 3 meV. This value was confirmed by a relativistic *R*-matrix calculation [39], whereas the spin-orbit splitting predicted at the RTDDFT level is less than the experimental one by about one order of magnitude. This discrepancy can be attributed to the LB94 XC potential used. Above the $^2D_{5/2}$ threshold there are three Rydberg series, namely, those associated with the discrete excitations Hg $5d^96s^2(^2D_{3/2})np_{1/2}$, $np_{3/2}$, $n'f_{5/2}$, which are reported for $n=7-9$ and for $n'=5$ in the same figure. Breaks are used in order to separate these two energy intervals. The calculated autoionization resonances have been characterized by fitting the theoretical profiles with a parametric form developed by Fano and Cooper [40], which, for an isolated resonance, take the following form:

$$\sigma=\sigma_0(1+a\varepsilon)\left[\rho^2\frac{(q+\varepsilon)^2}{(1+\varepsilon^2)}-\rho^2+1\right], \qquad (21)$$

where ε is the reduced energy

$$\varepsilon=\frac{2(E-E_R)}{\Gamma}.$$

The best-fit parameters have been computed by minimizing the squared deviations between the curve and the computed cross section. σ_0 is the background intensity, a is a coefficient for the background linear drift, ρ^2 is the correlation index, which is the ratio between the resonant intensity and the sum of resonant and nonresonant intensities, q is the Fano parameter which characterizes the line profile, Γ is the half-width, and E_R is the resonance energy. When m autoionization resonances were partially overlapped, the fitting procedure was performed with a modified parametrized curve obtained as product of m parametric forms of the type (21), with a quadratic background:

$$\sigma=\sigma_0[1+a(E-E_{\mathrm{ref}})+b(E-E_{\mathrm{ref}})^2]\times\prod_1^m\left[\rho_i^2\frac{(q_i+\varepsilon_i)^2}{(1+\varepsilon_i^2)}-\rho_i^2+1\right], \qquad (22)$$

where the various symbols have the same meanings as above specified whereas a, b, and E_{ref} are parameters that specify the background behavior.

The Fano parameters for the lowest members of the Rydberg series converging to the $^2D_{3/2}$ and $^2D_{5/2}$ ionization limits are collected in Tables I and II, respectively, together with the available experimental results of Garton and Connerade [41] and Brehm [38]. Good agreement between RTDDFT results and the experimental data of Brehm [38] is obtained for the $5d^96s^2(^2D_{3/2})6p_{1/2},p_{3/2}$ excitations, whereas a less satisfactory accord is found for the energy positions of the $5d^96s^2(^2D_{3/2})7p_{1/2},p_{3/2}$ excitations belonging to the same Rydberg series. Infact, their resonance energy calculated at the RTDDFT level disagrees with the absorption measurements of Garton and Connerade [41] by about 0.3 eV, but this gap is reduced at 0.1 eV for the subsequent members. A similar behavior is found when the RTDDFT energy resonances for the $5d^96s^2(^2D_{5/2})7p_{3/2}$ and $5d^96s^2(^2D_{5/2})8p_{3/2}$ autoionization resonances are compared with the values tabulated in [41] (Table II). The energy position for the $5d^96s^2(^2D_{3/2})5f_{5/2}$ excitation predicted at the RTDDFT level is in good agreement, within 0.15 eV, with the experimental data of Garton and Connerade [41] (Table I). The present results compare quite favorably with the only previous *ab initio* study of autoionization resonances in the energy interval between the $^2S_{1/2}$ and $^2D_{5/2}$ thresholds with a relativistic *R*-matrix approach [39]. The overall accord between RTDDFT results and experimental ones can be considered quite satisfactory, the discrepancies being ascribed to the deficiency of the LB94 XC potential used in the calculation.

In the lower panel of Fig. 11 we have reported the asymmetry parameter profile for the $^2S_{1/2}$ final ionic state either in the energy region between the $^2S_{1/2}$ and $^2D_{5/2}$ thresholds or between the $^2D_{5/2}$ and $^2D_{3/2}$ ones together with the experimental data available from the literature [42,43] for the $5d^96s^2(^2D_{3/2})6p_{1/2},p_{3/2}$ autoionization resonances. The asymmetry parameter profile fluctuates rapidly within the allowed range of $+2$ and -1 across each resonance. As can be seen, the accord between theoretical and experimental results is excellent for the $5d^96s^2(^2D_{3/2})6p_{3/2}$ autoionization resonance, and the present RTDDFT results constitute an important improvement over the earlier theoretical *R*-matrix results [39]. As can be seen, above the $^2D_{5/2}$ thresholds, the oscillation amplitude of the β parameter across the various members of the Hg $5d^96s^2(^2D_{3/2})np_{1/2}$, $np_{3/2}$, $n'f_{5/2}$ Rydbergs series are slightly decreasing with the photon energy.

Similar to cross sections and asymmetry parameter profiles, also the spin-polarization parameters display strong fluctuations across each autoionization resonance, as can be seen from Fig. 12, where the spin-polarization parameters ξ, A, and α are reported for the $^2S_{1/2}$ final ionic state either in the energy region between the $^2S_{1/2}$ and $^2D_{5/2}$ thresholds or between the $^2D_{5/2}$ and $^2D_{3/2}$ ones, together with the experimental data available from the literature [44–46]. As for the β_{6s} asymmetry parameter, the accord between RTDDFT results and experimental measurements [44,45] is excellent especially for the $5d^96s^2(^2D_{3/2})6p_{3/2}$ autoionization resonance, whereas at higher energies the experimental data are rather sparse. The opening of the $5d_{5/2}$ photoionization channels has an influence on the behavior of the ξ parameter which is characterized by wider oscillations across each member of the Hg $5d^96s^2(^2D_{3/2})np_{1/2,3/2}$ $n'f_{5/2}$ autoionization resonances than that observed for the lowest member of these Rydberg series. The opposite behavior is instead observed for the A parameter. In this energy interval the RTDDFT results are compared with the experimental results of Müller *et al.* [46]. For both the ξ and A spin-polarization parameters, the experimental variation across the Hg

TABLE I. Theoretical and experimental values of Fano parameters.

	Relative to the three lowest $5d^9(^2D_{3/2})np_{1/2}$ autoionization resonances					
	RTDDFT	Expt.[a]	RTDDFT	Expt.[b]	RTDDFT	Expt.[b]
Parameter	$5d^9(^2D_{3/2})6p_{1/2}$		$5d^9(^2D_{3/2})7p_{1/2}$		$5d^9(^2D_{3/2})8p_{1/2}$	
Γ (meV)	147.285	205.0	10.448		3.187	
q	9.682		6.305		5.548	
σ_0 (Mb)			5.084		6.240	
E_R (eV)	11.019		15.137	14.875	15.843	15.743
a			0.170		4.037×10^{-2}	
b			8.507×10^{-6}		$-1.943\times10-4$	
ρ^2	1.00		0.483		0.455	
	Relative to the three lowest $5d^9(^2D_{3/2})np_{3/2}$ autoionization resonances					
	$5d^9(^2D_{3/2})6p_{3/2}$		$5d^9(^2D_{3/2})7p_{3/2}$		$5d^9(^2D_{3/2})8p_{3/2}$	
Γ (meV)	31.592	22.0	2.502		0.734	
q	7.091	6.0	5.567		5.606	
σ_0 (Mb)			5.084		6.240	
E_R (eV)	11.711	11.607	15.243	14.966	15.884	15.777
ρ^2	1.00		0.651		0.585	

	Relative to the lowest $5d^9(^2D_{3/2})nf_{5/2}$ autoionization resonance	
	RTDDFT	Expt.[b]
Parameter	$5d^9(^2D_{3/2})5f_{5/2}$	
Γ (meV)	3.480×10^{-3}	
q	144.216	
σ_0 (Mb)	6.753	
E_R (eV)	16.000	15.842
a	-2.264×10^{-6}	
ρ^2	0.672	

[a] Experimental values, Ref. [38].

[b] Experimental values, [41].

$5d^9 6s^2(^2D_{3/2})np_{1/2}, np_{3/2}$, $n=7,8$, discrete excitations seems to be rather well accounted for by the RTDDFT results, apart from a small energy shift of the theoretical profiles toward higher photon energies. However, the lack of experimental data for the ξ and α spin-polarization parameters prevents a more definitive analysis of the theoretical RTDDFT data.

TABLE II. Theoretical and experimental values of Fano parameters relative to the two lowest $5d^9(^2D_{5/2})np_{3/2}$ autoionization resonances.

	RTDDFT	Expt.[a]	RTDDFT	Expt.[a]
Parameter	$5d^9(^2D_{5/2})7p_{3/2}$		$5d^9(^2D_{5/2})8p_{3/2}$	
Γ (meV)	9.512		2.568	
q	25.678		41.065	
σ_0 (Mb)	0.664		0.340	
E_R (eV)	13.420	13.131	14.043	13.920
a	-6.712×10^{-3}		-4.07×10^{-3}	
ρ^2	0.751		0.570	

[a] Experimental values, Ref. [41].

F. Autoionization resonances converging to the $^2P_{1/2,3/2}$ thresholds

There are five different Rydberg series of autoionizating resonances converging to the $^2P_{3/2,1/2}$ thresholds, associated with excitation of a bound $5p$ electron to $ns_{1/2}$ and $n'd_{3/2,5/2}$ Rydberg states, according to the following scheme:

$$\text{Hg}\ \ 5p^5 5d^{10} 6s^2(^2P_{3/2})ns_{1/2}, n'd_{3/2}, n'd_{5/2},$$

$$\text{Hg}\ \ 5p^5 5d^{10} 6s^2(^2P_{1/2})ns_{1/2}, n'd_{3/2}.$$

Owing to the huge spin-orbit splitting of the $^2P_{3/2,1/2}$ thresholds, the Rydberg series of autoionizing resonances converging onto different ionic thresholds are well separated in energy.

The total RTDDFT photoionization cross section in the energy interval of the Hg $5p^5 5d^{10} 6s^2(^2P_{3/2})ns_{1/2}, n'd_{3/2,5/2}$ autoionization resonances is reported in the upper panel of Fig. 13. The theoretical profiles were characterized by the least-squares fitting procedure with the parametrized forms (21) and (22), and the minimized Fano parameters are collected in Table III for the two lowest $ns_{1/2}$ $(n=7,8)$ and for

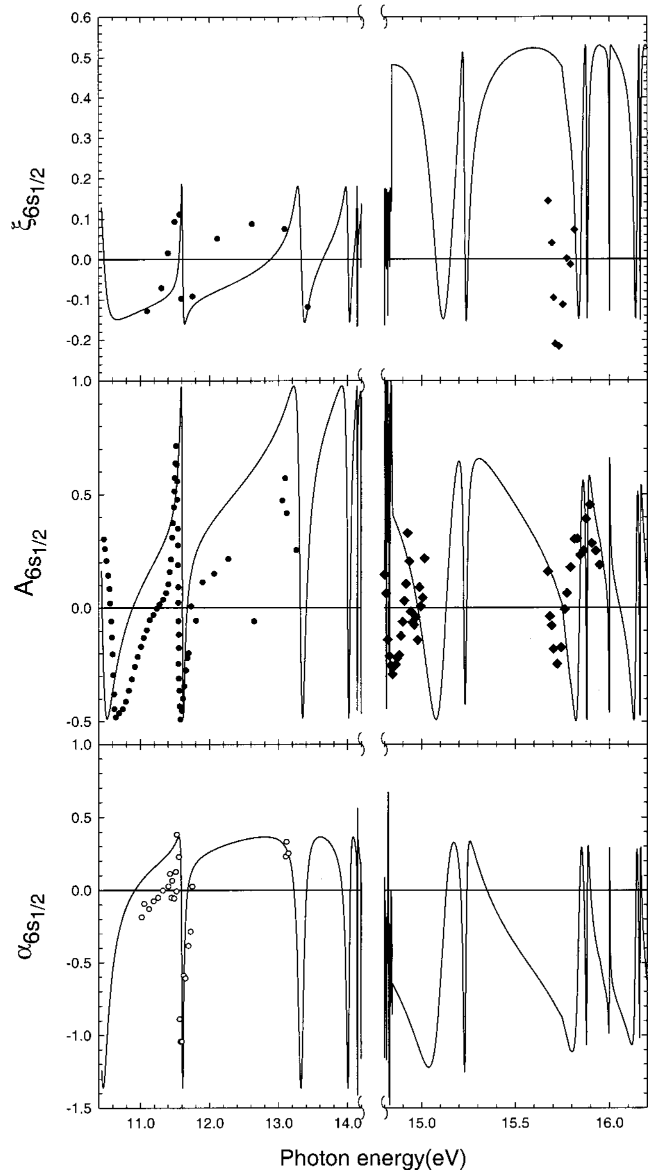

FIG. 12. Spin-polarization parameters for the $6s_{1/2}$ subshell in the autoionization region of $5d^9(^2D_{3/2})np_{1/2,3/2}n'f_{5/2}$ ($n=6-9$, $n'=5$) and $5d^9(^2D_{5/2})n''p_{3/2}$ ($n''=7,8$) configurations. Theory: solid lines, RTDDFT result. Experiment: closed circles from Ref. [44], open circles from Ref. [45], closed diamonds from Ref. [46].

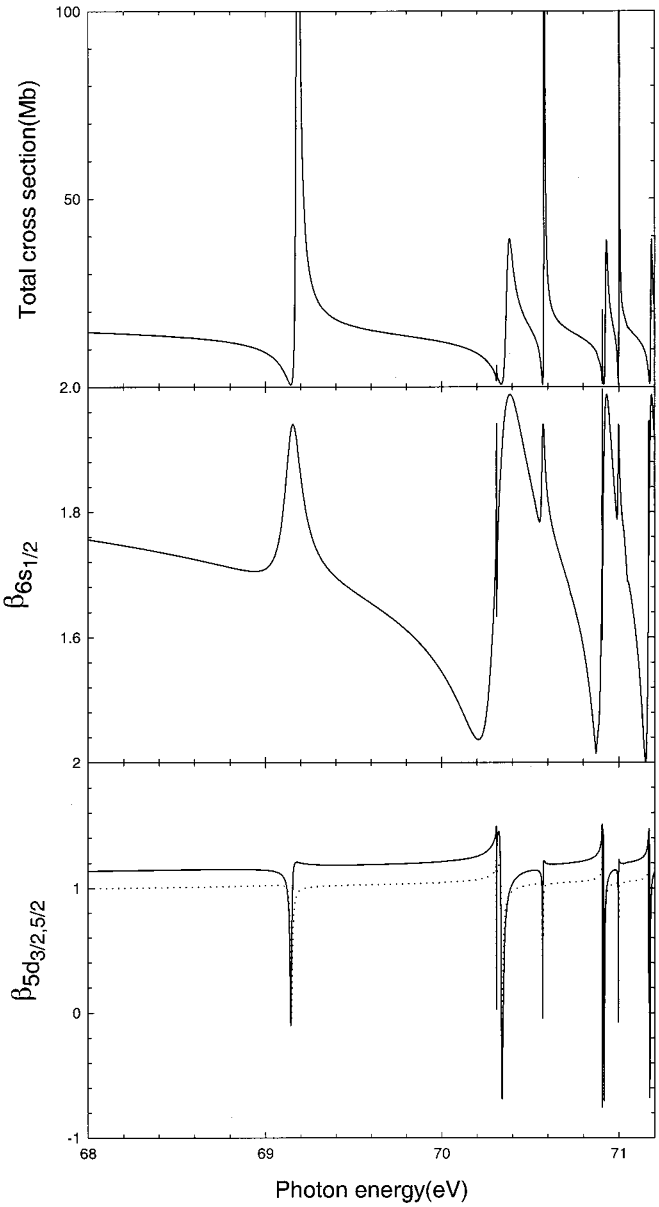

FIG. 13. *Upper panel.* Total RTDDFT photoionization cross-section profile in the autoionization region of $5p^5(^2P_{3/2})ns_{1/2}$ and $5p^5(^2P_{3/2})n'd_{3/2,5/2}$ configurations for $n=7-9$ and $n'=6,7$. *Central panel.* RTDDFT asymmetry parameter profile for the $6s_{1/2}$ subshell in the same spectral region. *Lower panel.* RTDDFT asymmetry parameter profile for the $5d_{3/2}$ (dotted line) and $5d_{5/2}$ (solid line) subshells of mercury in the same spectral region.

the lowest $n'd_{3/2,5/2}$ ($n'=6$) excitations, respectively. To our knowledge, no experimental data or other theoretical calculations are available from the literature for a comparison with the RTDDFT results. As can be seen from Fig. 13, the first member ($n=7$) of the Hg($^2P_{3/2}$)$ns_{1/2}$ excitations is well separated from the other, it displays a positive q value and is superimposed on a strong nonresonant background. The second member of this Rydberg series is strongly overlapping the lowest member of the other two Rydberg series, and for its characterization we have performed the least-squares fitting procedure with the parametric form (22) with $m=3$.

With respect to the first member it displays nearly the same values for the q index and for the ρ^2 correlation index, whereas its half-width is reduced by a factor of 4. Autoionizating resonances belonging to the remaining Hg ($^2P_{3/2}$)$nd_{3/2,5/2}$ Rydberg series are seen to be strongly overlapping. Infact, the computed resonance energies for the lowest pair differs by only 59 meV. Because of the small energy difference between these two excitations the corresponding resonant behavior of the total cross section is drastically influenced. Infact, in the energy interval between 70.3 and 70.5 eV a broad structure is preceded by another resonant structure of reduced intensity. The assignment of the features to the $5p^5(^2P_{3/2})6d_{5/2}$ and $5p^5(^2P_{3/2})6d_{3/2}$ discrete excitations, respectively, can readily be done by inspection of the eigen-

TABLE III. Theoretical RTDDFT values of Fano parameters.

Relative to the two lowest $5p^55d^{10}6s^2(^2P_{3/2})ns_{1/2}$ autoionization resonances		
Parameter	$5p^5(^2P_{3/2})7s_{1/2}$	$5p^5(^2P_{3/2})8s_{1/2}$
Γ (meV)	19.920	4.783
q	3.689	3.253
σ_0 (Mb)	13.670	15.172
E_R (eV)	69.181	70.580
ρ^2	0.965	0.960
a	-1.472×10^{-3}	1.086×10^{-3}
b		-0.163
Relative to the lowest $5p^55d^{10}6s^2(^2P_{3/2})nd_{3/2,5/2}$ autoionization resonances		
Parameter	$5p^5(^2P_{3/2})6d_{3/2}$	$5p^5(^2P_{3/2})6d_{5/2}$
Γ (meV)	0.369	42.297
q	-165.796	2.789
E_R (eV)	70.311	70.370
ρ^2	0.924	1.00

values of the $6d_{5/2,3/2}$ Rydberg states in the bound-state problem. For these two resonances the Fano parameters differ significantly. Infact, the computed half-width for the $6d_{3/2}$ discrete excitation is less than that of the other excitation by about two orders of magnitude. Its profile index q is predicted negative and with a large absolute value whereas it is positive and close to the value of 3 for the second resonance. In the central and lower panel of Fig. 13 we have reported the asymmetry parameter profiles for the three final ionic states $^2S_{1/2}$, $^2D_{3/2}$, and $^2D_{5/2}$. In correspondence with every autoionization resonance, the β parameter profiles display strong oscillations with periodic behavior. The asymmetry parameter profiles for the $^2D_{3/2,5/2}$ ionic states are very similar apart from a small shift at higher values for the $^2D_{5/2}$ one, whereas a completely different behavior is associated with the $6s$ photoionization, where the window-type structures visible across each resonance in the $5d_{3/2,5/2}$ photoionization channels are replaced by sharp peaks in the β parameter profile for the $6s_{1/2}$ photoemission.

Finally, we present in the upper panel of Fig. 14 the RTDDFT total cross-section profile in the autoionization region of Hg $5p^55d^{10}6s^2(^2P_{1/2})ns_{1/2},n'd_{3/2}$ configurations. Of the two Rydberg series, the sharper one is associated with excitations to $ns_{1/2}$ Rydberg states, whereas the other is associated with discrete excitations to $n'd_{3/2}$ states. In the lower panel of Fig. 14 we have reported the $\beta 6s$ asymmetry parameter profile in the same spectral region, whereas the $\beta 5d_{3/2,5/2}$ and $\beta 5p_{3/2}$ asymmetry parameter profiles are reported in the upper and lower panels of Fig. 15. The behavior of the asymmetry parameter is very similar for the $^2D_{3/2,5/2}$ final ionic states, which in turn differ substantially from that observed for the $6s$ and $5p_{3/2}$ photoionization channels. The Fano parameters obtained with the least-squares procedure are collected in Table IV for the three and two lowest terms of the Hg $5p^55d^{10}6s^2(^2P_{1/2})ns_{1/2}$ and Hg $5p^55d^{10}6s^2(^2P_{1/2})n'd_{3/2}$ Rydberg series, respectively. For the three lowest members ($n=7-9$) of the Hg $5p^55d^{10}6s^2(^2P_{1/2})ns_{1/2}$ autoionization resonances, the index profile q displays a positive value slightly decreasing in the series, and the same behavior is displayed by the correlation index ρ^2. A positive q value is also displayed by the two lowest terms ($n=6,7$) of the Hg $5p^55d^{10}6s^2(^2P_{1/2})nd_{3/2}$ Rydberg series, which is nearly the same for the two autoionizating resonances considered. Unfortunately, the lack of experimental and/or other theoretical investigations in the resonant regions below the $^2P_{1/2,3/2}$ thresholds prevent a further detailed analysis of the performance of the RTDDFT approach.

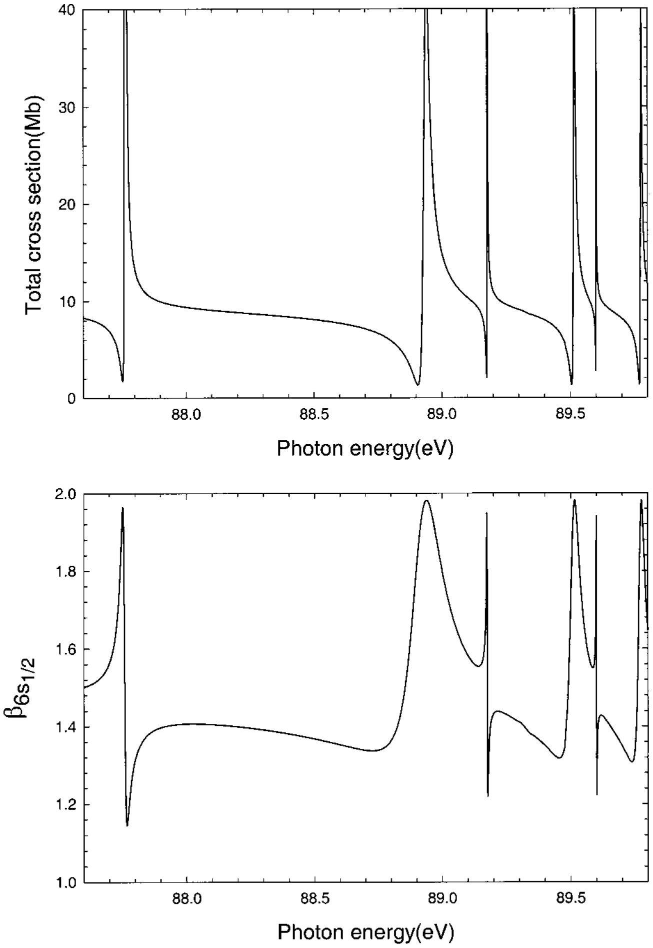

FIG. 14. *Upper panel.* Total RTDDFT photoionization cross-section profile in the autoionization region of $5p^5(^2P_{1/2})ns_{1/2}$ and $5p^5(^2P_{1/2})n'd_{3/2}$ configurations for $n=7-9$ and $n'=6,7$. *Lower panel.* RTDDFT asymmetry parameter profile for the $6s_{1/2}$ subshell in the same spectral region.

V. CONCLUDING REMARKS

In this work we have applied the RTDDFT formalism to the photoionization of mercury in a wide photon energy range, both in nonresonant and in resonant regions. All dynamical parameters, including spin polarization, have been considered.

An implementation of the RTDDFT equations with a noniterative procedure for the determination of the response

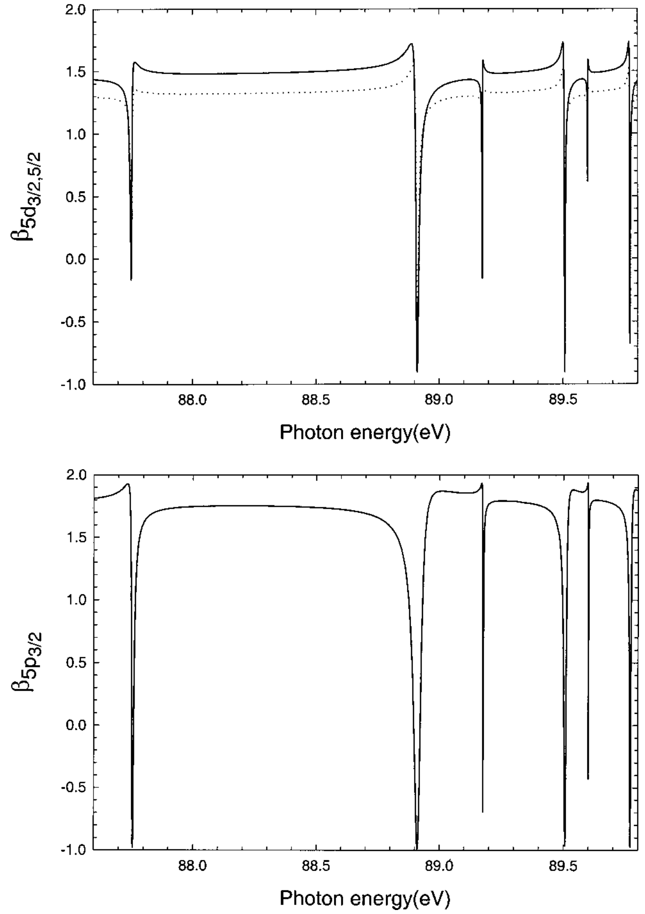

FIG. 15. *Upper panel*. Asymmetry parameter profile for the $5d_{3/2}$ (dotted line) and $5d_{5/2}$ (solid line) subshells of mercury in the autoionization region of $5p^5(^2P_{1/2})ns_{1/2}$ and $5p^5(^2P_{1/2})n'd_{3/2}$ configurations for $n=7-9$ and $n'=6,7$. *Lower panel*. RTDDFT asymmetry parameter profile for the $5p_{3/2}$ subshell in the same spectral region.

TABLE IV. Theoretical RTDDFT values of Fano parameters.

Relative to the three lowest $5p^55d^{10}6s^2(^2P_{1/2})ns_{1/2}$ autoionization resonances

Parameter	$5p^5(^2P_{1/2})7s_{1/2}$	$5p^5(^2P_{1/2})8s_{1/2}$	$5p^5(^2P_{1/2})9s_{1/2}$
Γ (meV)	2.611	0.562	0.257
q	7.575	7.384	7.119
σ_0 (Mb)	9.030		
E_R (eV)	87.763	89.177	89.600
ρ^2	0.809	0.792	0.790
a	-1.406×10^{-4}	-0.207	-0.508
b		6.263×10^{-6}	2.291×10^{-5}

Relative to the two lowest $5p^55d^{10}6s^2(^2P_{1/2})nd_{3/2}$ autoionization resonances

Parameter	$5p^5(^2P_{1/2})6d_{3/2}$	$5p^5(^2P_{1/2})7d_{3/2}$
Γ (meV)	24.997	7.746
q	2.216	2.194
E_R (eV)	88.934	89.514
ρ^2	0.850	0.850
a	-0.207	-0.508
b	6.263×10^{-6}	2.291×10^{-5}

induced potential together with the use of an exchange-correlation potential with correct asymptotic behavior has permitted, at RTDDFT level, the study of the Rydberg series of autoionization resonances converging to the $^2D_{3/2,5/2}$ and $^2P_{1/2,3/2}$ thresholds.

In every instance, comparison of the RTDDFT results with the experimental data and with other theoretical calculations (mainly RRPA and RRPAR) reveals that RTDDFT is at least as accurate as the computationally more expensive RRPA method. Agreement with experimental data is generally very satisfactory, although in some energy regions there are indications of discrepancies attributed to the neglect of additional many-electron interactions not taken into account in the present scheme.

Generally, an excellent description of autoionization resonances is obtained for all the photoionization dynamical parameters as demonstrated by the satisfactory accord with the experimental data when available from the literature.

In conclusion, this work has confirmed the high level of accuracy attainable with the RTDDFT approach in the description of the photoionization of heavy systems in a wide photon energy range. Therefore the generalization of the algorithm proposed for the resolution of the RTDDFT equations to the molecular case will constitute an important goal for the description of molecular photoionization processes.

ACKNOWLEDGMENT

This work was partially supported by grants from MURST of Italy.

---

[1] M. Ya Amusia and N. A. Cherepkov, Case Stud. At. Phys. **5**, 47 (1975).
[2] A. Zangwill and P. Soven, Phys. Rev. A **21**, 1561 (1980).
[3] W. R. Johnson and C. D. Lin, Phys. Rev. A **20**, 964 (1979).
[4] F. A. Parpia and W. R. Johnson, J. Phys. B **17**, 531 (1984).
[5] D. Toffoli, M. Stener, and P. Decleva, J. Phys. B **35**, 1275 (2002).
[6] A. K. Rajagopal, J. Phys. C **11**, L943 (1978).
[7] R. van Leeuwen and E. J. Baerends, Phys. Rev. A **49**, 2421 (1994).
[8] K.-N. Huang, Phys. Rev. A **22**, 223 (1980).
[9] G. D. Mahan and K. R. Subbaswamy, *Local Density Theory of Polarizability* (Plenum, New York, 1990).
[10] S. H. Vosko, L. Wilk, and M. Nusair, Can. J. Phys. **58**, 1200 (1980).
[11] C. de Boor, *A Practical Guide to Splines* (Springer, New York, 1978).
[12] C. Froese Fischer and M. Idrees, Comput. Phys. **3**, 53 (1989).

[13] C. Froese Fischer and F. A. Parpia, Phys. Lett. A **179**, 198 (1993).

[14] C. Froese Fischer, W. Guo, and Z. Shen, Int. J. Quantum Chem. **42**, 849 (1992).

[15] M. Stener, P. Decleva, and A. Lisini, J. Phys. B **28**, 4973 (1995).

[16] R. B. Cairns, H. Harrison, and R. I. Schoen, J. Chem. Phys. **53**, 96 (1970).

[17] J. L. Dehmer and J. Berkowitz, Phys. Rev. A **10**, 484 (1974).

[18] W. R. Johnson, V. Radojevic, P. Deshmukh, and K. T. Cheng, Phys. Rev. A **25**, 337 (1982).

[19] M. Kutzner, C. Tidwell, S. E. Vance, and V. Radojevic, Phys. Rev. A **49**, 300 (1994).

[20] S. P. Shannon and K. Codling, J. Phys. B **11**, 1193 (1978).

[21] F. A. Parpia and W. R. Johnson, J. Phys. B **16**, L375 (1983).

[22] M. D. W. Mansfield, Astrophys. J. **180**, 1011 (1973).

[23] S. Suzer, S. T. Lee, and D. A. Shirley, Phys. Rev. A **13**, 1842 (1976).

[24] J. Berkowitz, J. L. Dehmer, Y. K. Kim, and J. P. Desclaux, J. Chem. Phys. **61**, 2556 (1974).

[25] F. Schäfers, Ch. Heckenkamp, M. Müller, V. Radojevíc, and U. Heinzmann, Phys. Rev. A **42**, 2603 (1990).

[26] S. Süzer, P. R. Hilton, N. S. Hush, and S. Nordholm, J. Electron Spectrosc. Relat. Phenom. **12**, 357 (1977).

[27] D. W. Lindle, T. A. Ferret, P. A. Heimann, and D. A. Shirley, Phys. Rev. A **34**, 1131 (1986).

[28] W. R. Johnson and V. Radojevíc, Phys. Lett. A **92A**, 75 (1982).

[29] P. H. Kobrin, P. A. Heimann, H. G. Kerkhoff, D. W. Lindle, C. M. Truesdale, T. A. Ferret, U. Becker, and D. A. Shirley, Phys. Rev. A **27**, 3031 (1983).

[30] D. C. Frost, C. A. McDowell, and D. A. Vroom, Chem. Phys. Lett. **1**, 93 (1967).

[31] T. E. H. Walker and J. T. Waber, J. Phys. B **7**, 674 (1974).

[32] B. H. McQuaide, M. S. Banna, P. Gerard, and M. O. Krause, Phys. Rev. A **35**, 1603 (1987).

[33] A. Niehaus and M. W. Ruf, Z. Phys. **252**, 84 (1972).

[34] G. Schönhense, J. Phys. B **14**, L187 (1981).

[35] G. Schönhense, U. Heinzmann, J. Kessler, and N. A. Cherepkov, Phys. Rev. Lett. **48**, 603 (1982).

[36] G. Schönhense, F. Schäfers, U. Heinzmann, and J. Kessler, Z. Phys. A **304**, 31 (1982).

[37] F. Schäfers, Ch. Heckenkamp, G. Schönhense, and U. Heinzmann, J. Phys. B **21**, 769 (1988).

[38] B. Brehm, Z. Naturforsch. A **21A**, 196 (1966).

[39] K. Bartschat and P. Scott, J. Phys. B **18**, L191 (1985).

[40] U. Fano and J. W. Cooper, Phys. Rev. A **137**, A1364 (1965).

[41] W. R. S. Garton and J. P. Connerade, Astrophys. J. **155**, 667 (1969).

[42] B. Brehm and K. Höfler, Phys. Lett. A **68A**, 437 (1978).

[43] N. L. S. Martin, Nucl. Instrum. Methods Phys. Res. B **40/41**, 228 (1989).

[44] F. Schäfers, G. Schönhense, and U. Heinzmann, Z. Phys. A **304**, 41 (1982).

[45] G. Schönhense, F. Schäfers, Ch. Heckenkamp, U. Heinzmann, and M. A. Baig, J. Phys. B **17**, L771 (1984).

[46] M. Müller, F. Schäfers, N. Böwering, Ch. Heckenkamp, and U. Heinzmann, Phys. Scr. **35**, 459 (1987).